JOURNAL OF SOLID STATE CHEMISTRY 115, 324–331 (1995)

Structural Characterization of $R_2Cu_2O_5$ (R = Yb, Tm, Er, Y, and Ho) Oxides by Neutron Diffraction

J. L. García-Muñoz* and J. Rodríguez-Carvajal†

*Institut de Ciència de Materials de Barcelona, CSIC, Campus UAB, 08193 Bellaterra, Spain; and †Laboratoire Léon Brillouin, 91191 Gif sur Yvette Cedex, France

Received April 19, 1994; accepted August 3, 1994

The structural features of the $R_2Cu_2O_5$ family of compounds have been studied by high-resolution neutron powder diffraction. This isostructural series belongs to the noncentrosymmetric space group $Pna2_1$. A comparative study of the influence of the rare earth on the structural parameters is presented. In addition to the expected expansion of the RO_6 octahedra when the rare earth ionic radii are varied, the main modification of the structure corresponds to the elongation of the apical Cu–O distance in the CuO_5 pyramid. Conversely, the basal plane remains unchanged. A systematic variation of the structural stability is found depending on the size of the rare earth atom.

INTRODUCTION

In the ternary R–Cu–O (R = rare earth) phase diagram, the orthorhombic La_2CuO_4-type structure (T) leads to the p-type superconductors (1). For small R (from Pr to Gd) the crystal structure corresponds to the T′ type with Cu ions having square planar coordination. This structure permits the injection of electrons in the Cu planes by Ce or Th doping, given the still not very well understood n-type superconductivity (2). The metastable T* structure occurs in a very narrow region at the boundary T/T′ resulting from a thermodynamic competition between T and T′ structures (3). Finally, the R_2CuO_4 composition is no longer stable at atmospheric pressure for a rare earth smaller than Gd. For Gd_2CuO_4, a recent structure analysis shows a long-range superstructure of the T′ phase (space group $Acam$) (4). Then the $R_2Cu_2O_5$ crystal structure arises for the heavier rare earths. For tolerance factors $t < 0.83$ ($t = d_{R-O}/\sqrt{2}d_{Cu-O}$) (3) only $R_2Cu_2O_5$ compounds with sixfold-coordinated R sites are known at ambient pressures. According to these tolerance factors, the segregation of the T, T*, T′, and 2:2:5 phases (3) can be attributed to the breakdown of the R–O coordination number as the rare earth size decreases. Within the ionic model, the variations of the rare coordination number are due to electrostatic requirements, in an attempt to optimize the Madelung energy of the R–O framework. The instability is reflected by the different rare earth coordinations: ninefold in T, eightfold in T′, and sixfold in $R_2Cu_2O_5$.

The so-called "blue phases" crystallize in the orthorhombic space group $Pna2_1$. The first X-ray diffraction investigations on this structure are those in Refs. (5, 6). In 1977, Freund *et al.* synthesized the first single crystal of this family, $Ho_2Cu_2O_5$ (6), and confirmed the structure previously reported by Bergerhoff (5). During the past years, structure refinements of some $R_2Cu_2O_5$ compounds from neutron powder diffraction studies have been published (7–9).

The structure can be thought of as a stack of Cu–O layers aligned parallel to the ab-plane and separated by layers of rare earth atoms (Fig. 1). There are two nonequivalent fourfold low symmetry positions for Cu^{2+} and R^{3+}, but both have very similar oxygen polyhedra. There is a distorted square planar arrangement around copper, with a fifth oxygen making a sort of pyramid with a "diagonal broken" CuO_4 "square." These copper–oxygen pyramids are joined at the common edges into Cu_2O_8 dimers which, in turn, form infinite zigzag Cu_2O_5 chains along the a-axis. Furthermore, each Cu is coupled to four other Cu ions along the b-axis forming ab-pseudoplanes, and intraplane distances are considerably smaller than interplane ones. The rare earth ions are octahedrally coordinated, and RO_6 distorted octahedra are linked in a three-dimensional network occupying the space between copper planes.

There are magnetic transitions in copper and rare earth sublattices in most of these compounds below 30 K. The discussion of their magnetic properties can be found elsewhere (10). An effort to understand the crystal chemistry and phase stability of the $R_2Cu_2O_5$ family has been undertaken. In the present work we have analyzed the structural details of these oxides in a comparative way. All structural data were obtained from high-resolution neutron powder diffraction measurements. The main goal is to determine the variation of the relevant geometrical parameters as a function of the rare earth ion size. This is a preliminary step to the understanding of their microscopic magnetic properties.

0022-4596/95 $6.00

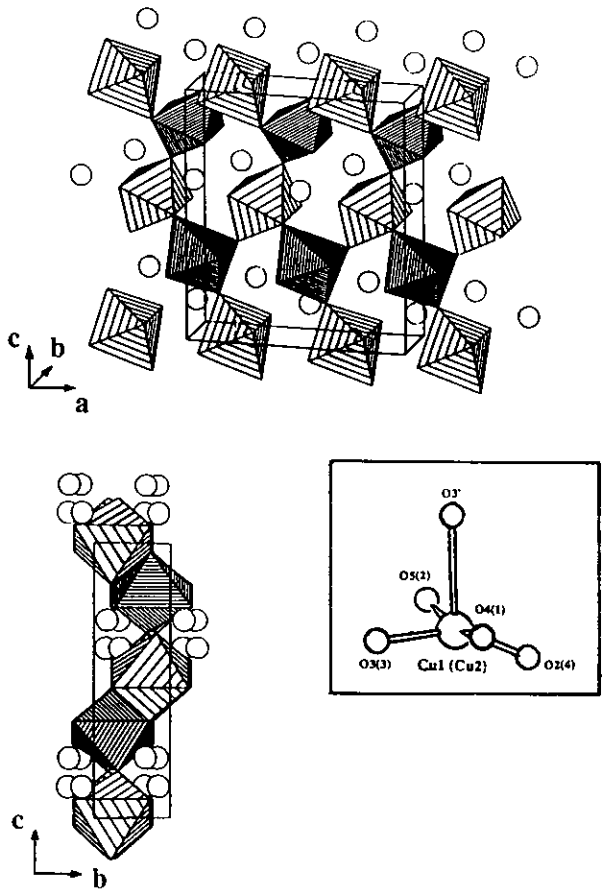

FIG. 1. Schematic representation of the crystal structure of $R_2Cu_2O_5$ showing the RO_6 octahedra separating the CuO layers. Inset: coordination polyhedra of Cu^{2+} ions (see the relevant distances and angles in Tables 3 and 4).

EXPERIMENTAL DETAILS

Ceramic synthesis of $R_2Cu_2O_5$ with R = Yb, Tm, Er, Y, and Ho has been done by heating in air stoichiometric amounts of high purity oxides R_2O_3 (99.99%) and CuO (99.999%) at T = 950°C. Several intermediate grindings were carried out to homogenize the reaction products. The total firing time was about 12 days in order to get a complete reaction of the starting oxides.

Neutron powder diffraction experiments were carried out in the high flux reactor of the Institut Laue–Langevin in Grenoble. All the diffraction patterns were recorded on the high-resolution powder diffractometer D2B with a wavelength λ = 1.594 Å. The instrument was used in its high flux mode of operation. This diffractometer is equipped with a bank of 64 detectors separated by 2.5° in 2Θ, spanning an angular range of 160°. Each detector is equipped with Soller slits. The step size for the measurements was 0.05° and the angular range was 0°–160° (2Θ). Most of the data were collected at room temperature, otherwise the temperature is indicated. The high-resolution patterns, covering a wide range of angles, allowed us to study fine structural details. In particular, the oxygen positions can be determined with high accuracy as compared to data obtained with X-ray techniques.

The diffraction data were analyzed with the Rietveld method, using the program "FULLPROF" (11). The pseudo-Voigt profile function was used in the refinements, which show no preferential orientation of the crystallites.

RESULTS

A very small amount of R_2O_3 was detected in some cases and included as an impurity phase in the refinements ($R_2O_3 \lesssim 3.6\%$). The diffraction patterns were refined in the noncentrosymmetric space group $Pna2_1$ from the starting

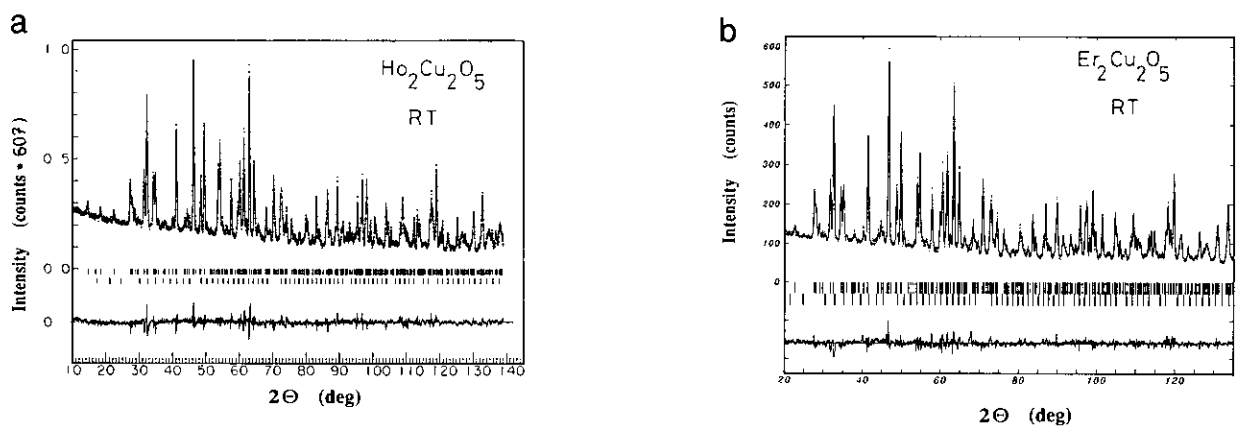

FIG. 2. Observed and calculated neutron diffraction patterns (space group $Pna2_1$) for (a) $Ho_2Cu_2O_5$ and (b) $Er_2Cu_2O_5$. The difference curve is also plotted at the bottom of each frame. The second row of marks corresponds to R_2O_3 impurity.

TABLE 1
Lattice Parameters (Å) and Reliability Factors for $R_2Cu_2O_5$ Compounds from High-Resolution Neutron Diffraction Data

	Lattice parameters (Å)					Reliability factors (%)			
	a	b	c	V (Å^3)	Number of reflections	R_{wp}	R_{exp}	χ^2	R_{Bragg}
$Tb_2Cu_2O_5$[a]	10.856	3.544	12.530	482.1					
$Dy_2Cu_2O_5$[a]	10.830	3.514	12.465	474.3					
$Ho_2Cu_2O_5$	10.8096(2)	3.4962(1)	12.4735(2)	471.41	477	13.5	9.3	2.1	6.0
$Y_2Cu_2O_5$[b]	10.796(2)	3.494(1)	12.4546(2)	469.80	431	8.5	3.3	2.1	5.6
$Er_2Cu_2O_5$	10.7839(2)	3.4745(1)	12.4434(3)	466.24	461	6.2	4.1	2.2	6.7
$Tm_2Cu_2O_5$[c]	10.7353(1)	3.4575(1)	12.3704(2)	459.2	475	8.1	3.2	6.5	6.4
$Yb_2Cu_2O_5$	10.7290(1)	3.4355(1)	12.3531(1)	455.33	469	11.0	5.5	4.0	4.2
$Lu_2Cu_2O_5$[a]	10.709	3.413	12.363	451.9					
$In_2Cu_2O_5$[a]	10.546	3.273	12.280	423.9					
$Sc_2Cu_2O_5$[a]	10.438	3.219	12.036	404.4					

[a] From Ref. (9).
[b] 80 K.
[c] 1.5 K.

values of $Y_2Cu_2O_5$ in the literature. Any attempt to find a centrosymmetric description of the structure was unsuccessful. The crystal structure is well represented by the model first proposed by Freund and Müller-Buschbaum. Absorption corrections were included in the refinements for some rare earths (when necessary). In Fig. 2 the observed and calculated patterns for $Ho_2Cu_2O_5$ and $Er_2Cu_2O_5$ are shown. The lattice parameters and usual reliability factors are given in Table 1 for the different $R_2Cu_2O_5$ oxides. For the purpose of comparison, in this table we have also included the lattice parameters for the larger R = Tb, Dy and the smaller R = Lu, In, Sc ions obtained from X-ray powder diffraction (from Ref. 9). In the table they have been ordered relative to their rare earth size.

As expected, assuming the ionic model, the lattice parameters a, b, and c of the unit cell decrease linearly as a function of the lanthanide ionic radius r_0 (12) going from Tb^{3+} ($r_0 \approx 1.040$ Å) to Sc^{3+} ($r_0 \approx 0.870$ Å). This has been represented in Fig. 3a, and the linear evolution of the volume vs r_0^3 is shown in Fig. 3b.

In the space group $Pna2_1$ there is only one Wyckoff

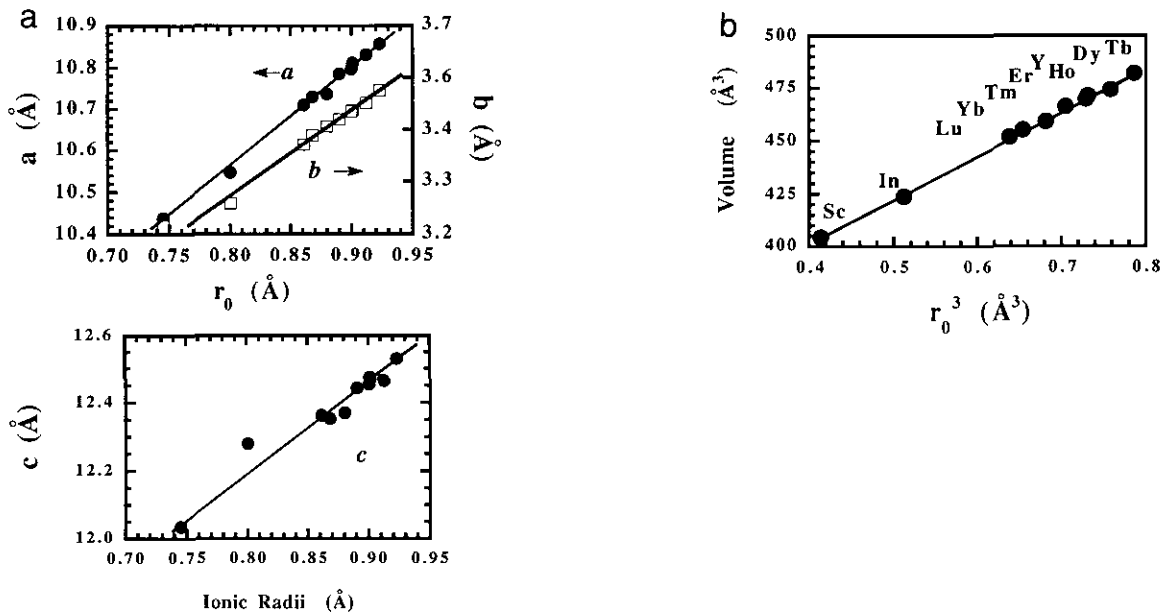

FIG. 3. (a) Variation of the lattice parameters a, b, and c vs ionic radii for the different $R_2Cu_2O_5$ oxides. (b) Variation of the unit cell volume vs the third powder of the ionic radii. Solid lines are a visual guide.

TABLE 2
Refined Atomic Coordinates and Isotropic Temperature Factors for $R_2Cu_2O_5$ (R = Ho, Y, Er, Tm, and Yb) Oxides

		$Ho_2Cu_2O_5$	$Y_2Cu_2O_5$[a]	$Er_2Cu_2O_5$	$Tm_2Cu_2O_5$[b]	$Yb_2Cu_2O_5$
R(1)	*x*	*0.208(1)*	*0.2067(7)*	*0.207(1)*	*0.208(1)*	*0.2088(6)*
	y	0.227(1)	0.231(1)	0.226(2)	0.234(1)	0.2269(7)
	z	0	0	0	0	0
	B (Å^2)	0.4(1)	0.3(1)	0.9(1)		0.3(1)
R(2)	*x*	0.0424(8)	0.0406(7)	0.0414(9)	0.040(1)	0.0416(6)
	y	0.226(1)	0.232(1)	0.222(1)	0.225(1)	0.2231(6)
	z	0.3303(3)	0.3294(3)	0.3300(4)	0.3308(3)	0.3304(2)
	B (Å^2)	0.4(1)	0.3(1)	0.9(1)		0.3(1)
Cu(1)	*x*	0.9902(5)	0.9909(4)	0.9911(8)	0.9892(4)	0.9907(4)
	y	0.662(2)	0.656(2)	0.653(2)	0.650(2)	0.661(1)
	z	*0.115(1)*	*0.1123(9)*	*0.112(1)*	*0.114(1)*	*0.113(1)*
	B (Å^2)	0.9(1)	0.6(1)	1.3(1)		0.5(1)
Cu(2)	*x*	0.2610(5)	0.2602(4)	0.2593(7)	0.2598(4)	0.2608(4)
	y	0.664(2)	0.674(2)	0.669(2)	0.672(1)	0.661(2)
	z	0.217(1)	0.2151(9)	0.215(1)	0.216(1)	0.217(1)
	B (Å^2)	0.9(1)	0.6(1)	1.3(1)		0.5(1)
O(1)	*x*	0.173(1)	0.1761(9)	0.176(1)	0.173(1)	0.174(1)
	y	0.726(2)	0.723(2)	0.727(3)	0.724(2)	0.729(2)
	z	0.359(1)	0.3487(9)	0.357(1)	0.358(1)	0.357(1)
	B (Å^2)	0.4(2)	0.2(1)	0.7(2)		0.1(2)
O(2)	*x*	*0.324(1)*	*0.3262(7)*	*0.322(1)*	*0.323(1)*	*0.323(1)*
	y	0.712(3)	0.733(2)	0.713(3)	0.722(2)	0.718(2)
	z	0.066(1)	0.0665(8)	0.059(1)	0.065(1)	0.064(1)
	B (Å^2)	1.6(3)	0.5(3)	1.5(3)		0.4(2)
O(3)	*x*	0.124(1)	0.123(1)	0.124(2)	0.127(1)	0.125(1)
	y	0.320(2)	0.314(2)	0.319(2)	0.304(1)	0.313(1)
	z	0.169(1)	0.165(1)	0.167(2)	0.167(1)	0.165(1)
	B (Å^2)	1.0(1)	0.7(1)	1.2(1)		0.6(1)
O(4)	*x*	0.427(1)	0.431(1)	0.427(1)	0.428(1)	0.428(1)
	y	0.776(2)	0.781(2)	0.773(2)	0.776(2)	0.778(2)
	z	*0.263(1)*	*0.263(1)*	*0.259(1)*	*0.262(1)*	*0.263(1)*
	B (Å^2)	0.2(2)	0.3(2)	0.2(2)		0.3(2)
O(5)	*x*	0.426(1)	0.4241(9)	0.424(2)	0.424(1)	0.425(2)
	y	0.230(2)	0.236(2)	0.227(3)	0.228(2)	0.228(3)
	z	0.479(1)	0.470(1)	0.476(1)	0.477(1)	0.476(2)
	B (Å^2)	0.9(2)	0.5(2)	1.1(3)		0.9(3)

[a] 80 K.
[b] 1.5 K.

position of fourfold multiplicity and site symmetry 1. Due to the indetermination in the *z* coordinate we have selected arbitrarily $z = 0$ for the $R(1)$ site. The refined atomic coordinates for the nine nonequivalent occupied atomic sites in the $Pna2_1$ space group are given in Table 2, together with the isotropic temperature factors. As expected, the atomic coordinates obtained for each atom of the asymmetric unit are very close in all these oxides. For $Ho_2Cu_2O_5$ our results are practically identical to those first determined by Freund and Müller-Buschbaum from single crystal X-ray data (6). Very few differences are observed when looking at the coordinates of oxygen ions, and our oxygen coordinates agree very well with previous powder neutron diffraction data reported by Murasik *et al.* in Ref. (14). A good agreement is also found with the neutron data by Aride *et al.* for $Y_2Cu_2O_5$ in Ref. (8).

In Table 3 we give the interatomic cation–oxygen distances for the coordination polyhedra of Cu and R ions. The main angles of these polyhedra are listed in Table 4. It is worth emphasizing that, even if two unequivalent copper positions do exist in the orthorhombic cell, they are practically equally coordinated: there is a distorted square planar arrangement ($d_{Cu-O} \approx 1.97$ Å) and a fifth oxygen at a distance of 2.7 Å, making a sort of pyramid with a strongly distorted square base. The distortion of the oxygen square plane around copper is shown in detail in Fig. 1. Both angles and distances are very similar

TABLE 3
Main Interatomic Distances (Å) for $R_2Cu_2O_5$ (R = Ho, Y, Er, Tm, and Yb) Oxides

	$Ho_2Cu_2O_5$	$Y_2Cu_2O_5$	$Er_2Cu_2O_5$	$Tm_2Cu_2O_5$	$Yb_2Cu_2O_5$
			Pyramids		
Cu(1)–O(2)	1.95(1)	1.90(1)	2.00(1)	1.94(2)	1.94(1)
–O(3)	1.99(1)	1.98(1)	1.97(1)	2.01(1)	1.98(1)
–O(4)	1.98(1)	1.99(2)	1.97(1)	1.95(2)	1.98(2)
–O(5)	1.93(1)	2.02(1)	1.94(1)	1.95(2)	1.93(2)
–O(3′)	2.80(1)	2.78(1)	2.81(1)	2.78(1)	2.74(1)
Cu(2)–O(4)	1.93(1)	1.97(1)	1.92(1)	1.92(2)	1.92(1)
–O(3)	2.00(1)	2.04(1)	1.99(1)	2.00(1)	1.99(1)
–O(1)	2.02(1)	1.90(1)	1.99(1)	1.99(2)	1.99(1)
–O(2)	2.01(2)	1.99(1)	2.06(1)	2.00(2)	2.00(2)
–O(3′)	2.80(1)	2.78(1)	2.75(1)	2.68(1)	2.75(1)
Basal plane ⟨Cu–O⟩	1.976(9)	1.974(9)	1.980(9)	1.970(9)	1.966(9)
Apical distance ⟨Cu–O(3′)⟩	2.80(1)	2.78(1)	2.78(1)	2.73(1)	2.74(1)
			Octahedra		
R(1)–O(1)	2.18(2)	2.27(1)	2.18(1)	2.16(2)	2.17(1)
–O(2)	2.33(1)	2.32(1)	2.29(1)	2.30(1)	2.28(1)
–O(2)	2.26(1)	2.33(1)	2.22(1)	2.24(1)	2.24(1)
–O(3)	2.31(1)	2.27(1)	2.28(2)	2.26(2)	2.25(1)
–O(5)	2.29(1)	2.27(1)	2.26(1)	2.24(1)	2.25(1)
–O(5)	2.30(1)	2.29(1)	2.26(1)	2.27(1)	2.26(1)
R(2)–O(1)	2.27(1)	2.31(1)	2.28(1)	2.27(1)	2.24(1)
–O(3)	2.23(1)	2.25(2)	2.25(1)	2.25(2)	2.25(1)
–O(4)	2.31(1)	2.30(1)	2.29(2)	2.28(1)	2.27(1)
–O(5)	2.24(1)	2.15(1)	2.23(1)	2.20(2)	2.20(1)
–O(4)	2.31(1)	2.23(1)	2.32(1)	2.27(1)	2.26(1)
–O(1)	2.27(1)	2.27(1)	2.30(1)	2.27(1)	2.27(1)
⟨R–O⟩	2.275(4)	2.272(4)	2.265(6)	2.250(5)	2.243(5)

around Cu(1) and Cu(2). The two different pairs of ≈180° O–Cu–O bonded oxygen atoms are displaced up and down respectively from the plane at the copper site perpendicular to the axial Cu–O(3′) bond (the prime symbol signifies the oxygen involved in the longest Cu–O bond around copper). Displacements are within the range −0.1 to 0.3 Å, except one oxygen bonding the dimeric units, which is displaced 0.7 Å (≈22°). Thus, the four strongest bonded oxygens display a tetrahedral-like distortion. The data in Tables 3 and 4 also show very strong similarity between the octahedrally coordinated R(1) and R(2) sites. R–O distances vary from 2.15(1) to 2.33(1) Å.

Each CuO_4 square shares an edge with another CuO_4 square along a. The link among different dimers in the chains comes through sharing one of the longest edges O(3′)–O(3) of the coordination pseudopyramid. R(1) and R(2) polyhedra are linked by common O–O edges forming chains along b, which in turn, give rise to a three-dimensional structure with channels occupied by the Cu_2O_6 chains parallel to a.

Finally, each Cu is linked by O(3) atoms to the copper ions along b. This coupling involves the fifth oxygen bonding (O(3′)) in one sense parallel to b, and a short copper–oxygen distance in the other.

Therefore, an important feature of the crystal structure of the $R_2Cu_2O_5$ compounds in relation to their magnetic behavior is the existence of a hierarchy of exchange pathways: (i) intradimer and (ii) interdimer exchange paths (both through Cu–O–Cu nearly 90° bonded); (iii) intraplane interchain Cu–O(3)–Cu coupling, involving 91° and 162° angles; and finally (iv) interchain, interplane superexchange Cu–O–R–O–Cu paths. In Table 5 we have listed the values of the angles for Cu–O–Cu bonds propagating the magnetic interactions.

TABLE 4
Main Angles (°) in the Coordination Polyhedra of *R* (Octahedra) and Cu (Pyramids) of $R_2Cu_2O_5$ (*R* = Ho, Y, Er, Tm, and Yb) Oxides

	$Ho_2Cu_2O_5$	$Y_2Cu_2O_5$	$Er_2Cu_2O_5$	$Tm_2Cu_2O_5$	$Yb_2Cu_2O_5$
		Pyramids			
O(3')–Cu(1)–O(2)	111(1)	112(1)	110(2)	112(1)	112(1)
–O(3)	92(1)	92(1)	92(1)	91(1)	92(1)
–O(4)	82(1)	81(1)	81(1)	91(1)	83(1)
–O(5)	82(1)	82(1)	82(1)	81(1)	82(1)
O(3')–Cu(2)–O(4)	113(1)	112(1)	114(1)	114(1)	113(1)
–O(3)	92(1)	92(1)	93(1)	94(1)	91(1)
–O(1)	82(1)	82(1)	83(1)	83(1)	82(1)
–O(2)	85(1)	83(1)	85(1)	84(1)	83(1)
		Octahedra			
O(1)–*R*(1)–O(3)	165(6)	167(3)	165(7)	166(7)	166(5)
O(2)–*R*(1)–O(5)	165(4)	168(2)	168(4)	166(4)	166(3)
O(2)–*R*(1)–O(5)	165(4)	168(2)	168(5)	166(4)	166(3)
O(3)–*R*(2)–O(5)	163(5)	164(2)	163(5)	165(7)	163(5)
O(1)–*R*(2)–O(4)	167(4)	164(1)	165(4)	166(5)	166(3)
O(1)–*R*(2)–O(4)	167(4)	164(1)	165(6)	166(5)	166(3)

DISCUSSION

The careful analysis of the crystallographic data is very illustrative for better understanding the structural effects of the ionic radius variation of the trivalent rare earth (r_0).The same procedure used in the analysis of the R_2BaCuO_5 family (12) will be followed.

A systematic variation of the lattice parameters and cell volume is observed by changing the rare earth. We want now to identify the main modifications in the structure responsible for this behavior. First, there are no systematic changes either in the angles defining the coordination polyhedra around *R* and Cu cations (Table 4), nor in those angles connecting these polyhedra (Table 5). The next step is to examine the cation–oxygen distances. The evolution of the average planar Cu–O bond length in the CuO_5 pyramid of the "blue phases" can be visualized in Fig. 4. It is interesting to compare this distance with the Cu–O(3') (apex) distance as a function of the *R* ionic radii. Clearly, it can be observed that the basal plane of the copper pyramid remains almost constant in the different $R_2Cu_2O_5$ oxides (0.7% variation). On the other hand, there

TABLE 5
Exchange Angles (°) in the Topological Hierarchy of the Exchange Interactions in $R_2Cu_2O_5$

	$Ho_2Cu_2O_5$	$Y_2Cu_2O_5$	$Er_2Cu_2O_5$	$Tm_2Cu_2O_5$	$Yb_2Cu_2O_5$
Intradimer					
Cu(1)–O(4)–Cu(2)	93.6(8)	92.1(6)	95.3(10)	93.8(9)	93.6(7)
Cu(1)–O(2)–Cu(2)	92.1(8)	94.5(6)	90.4(10)	92.2(9)	92.5(7)
Interdimer					
Cu(2)–O(3')–Cu(1)	69.6(3)	70.1(2)	69.4(5)	70.9(3)	70.5(3)
Cu(2)–O(3)–Cu(1)	106.3(8)	104.7(3)	106.0(10)	104.2(7)	106.0(7)
Intraplane, interchain					
Cu(2)–O(3')–Cu(2)	91.9(5)	92.5(5)	92.9(8)	91.8(4)	91.5(4)
Cu(2)–O(3)–Cu(1)	161.7(9)	162.5(6)	160.9(4)	162.0(12)	161.9(7)

Note. Interplane superexchange angles are not included.

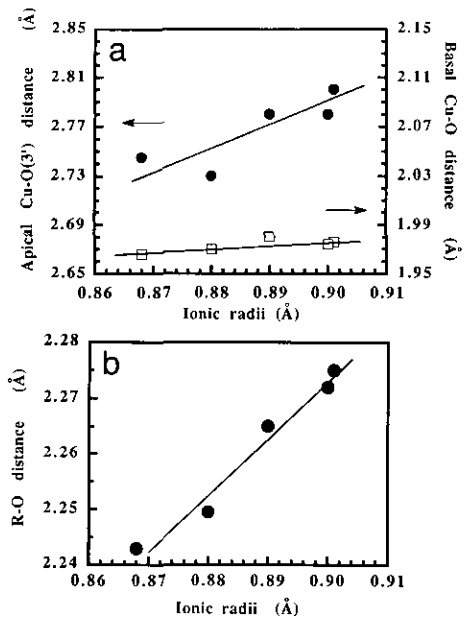

FIG. 4. (a) Evolution with the R ionic size of the Cu–O(3′) apex distance and the ⟨Cu–O⟩ basal distance of the CuO_5 pyramids in the $R_2Cu_2O_5$ family. (b) Evolution of the mean rare earth to oxygen distance in the RO_6 octahedra. Solid lines are a visual guide.

is a visible elongation of the apical Cu–O(3′) distance with a 2.5% variation from Yb to Ho (Δd[Cu–O(3′)] = 0.06 Å). This is very close to the size difference between rare earths at the two ends: 2* (r_0[Ho] − r_0[Yb]) ≈ 2* (0.901 − 0.868) = 0.06 Å. The R–O octahedra are also expanded from Yb to Ho by approximately the 1.5%. This variation, shown in Fig. 5, is just the expression of the r_0 value.

Furthermore, the CuO_5 pyramid in $R_2Cu_2O_5$ is much more elongated than in the R_2BaCuO_5 family ("green phase"). In this latter case the axial Cu–O bond length is about 2.2 Å (2.7 Å in "blue phases"). It is also worth

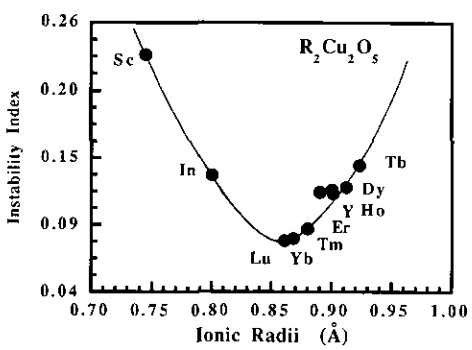

FIG. 5. Instability index of $R_2Cu_2O_5$ oxides vs the ionic radii. The values for R = Tb, Dy, Lu, In, and Sc have been calculated from data in Ref. (9). Solid lines are a visual guide.

TABLE 6
Valence Bond Sums (esd's ≈ 0.02 vu) Obtained for the Different $R_2Cu_2O_5$ (R = Ho, Y, Er, Tm, and Yb) Oxides

	$Ho_2Cu_2O_5$	$Y_2Cu_2O_5$	$Er_2Cu_2O_5$	$Tm_2Cu_2O_5$	$Yb_2Cu_2O_5$
Cu(1)	1.91	1.86	1.88	1.89	1.93
Cu(2)	1.78	1.85	1.79	1.83	1.85
⟨V[Cu]⟩	1.84	1.85	1.84	1.86	1.89
δV/V	8%	7.5%	8%	7%	5.5%
R(1)	3.04	2.86	3.15	3.11	3.04
R(2)	3.08	3.17	2.92	3.03	2.95
⟨V[R]⟩	3.06	3.02	3.04	3.07	3.00
δV/V	2%	0.7%	1.3%	2.3%	0%

emphasizing that the most relevant angles involved in the exchange magnetic interactions show no appreciable or systematic changes in the $R_2Cu_2O_5$ compounds (see Table 5).

For the purpose of completing the comparative study, we have applied the valence bond method for coming to some conclusions about their overall structural behavior. The phenomenological relation between the bond length and the valence of a bond can be expressed as $s_{ij} = \exp[(R_0 - R_{ij})/B]$ (13), where B = 0.37 is a "universal" constant and R_0 is a constant characteristic of the cation–anion pair. The valence sum rule (VSR) establishes that the sum of valence bonds around a cation (anion) must be equal to the formal valence (charge) of the i-cation (anion) (i.e., $\Sigma_j s_{ij} = V_i$). This method has been widely used by mineralogical crystallography for many years, giving very useful results because the VSR is verified, within a few percent, for many inorganic compounds. However, one of the bases of the VSR is that the structure should permit the release of the stress introduced by the coexistence of different structural units; i.e., the structure should have enough degrees of freedom. The case of $R_2Cu_2O_5$ oxides could be considered as belonging to the type of structures where the VSR should be fulfilled. By this method, the deviations of the valence sum around each ion with respect to the expected value can be estimated.

Accordingly, Table 6 shows the valence sum for the different $R_2Cu_2O_5$ oxides. Several conclusions can be drawn. First, the valence bond sums remain almost constant and very close to 3 for the rare earths. This is in accordance with the fact shown above that the average expansion of the RO_6 octahedra from Yb to Ho does correspond exactly to the ionic radii increment. Hence, the valence of these bonds is not altered. On another hand, the valence bond sums for Cu^{2+} give a value of ≈1.8 valence units (vu), lower than the theoretical value

of 2. This is a consequence of the Jahn–Teller effect shown by the Cu^{2+} ion. Nevertheless, the average valence of copper shows little overall increase as the ion size r_0 decreases. This is clearly associated with the elongation of the apical Cu–O(3′) bond in the pyramids, since the basal plane bonds of copper remain almost constant. Accordingly, with this elongation there is an overall decrease in the valence.

Finally the stability of the structure, in terms of the overall deviation of the VSM rule, has been investigated. The root mean square of the bond valence sum deviations for all the atoms present in the asymmetric unit is a measure of the extent to which the VSR is violated over the whole structure (15). We have called this value the "global instability index (GII)" (12),

$$\mathrm{GII} = \sqrt{\sum_{i=1}^{N} \left\{ \left(\sum_j s_{ij} - V_i \right)^2 \right\} \Big/ N}.$$

In Fig. 5 we have represented the variation of GII vs ionic radii of R for the $R_2Cu_2O_5$ family. It can be observed that minimum values (higher stability) are found for Lu and Yb. There is a monotonic evolution from the low values (higher stability) of these compounds to higher values (lower stability) for larger and smaller lanthanides. The rather symmetrical increase of the instability index at both sides is indicative of larger stress in the structure. Brown (15) and Armbruster *et al.* (16) have suggested that with GII values higher than 0.2 vu the intrinsic strains are large enough to cause instability at room temperature. In that case, the Tb and In compounds are still very far from instability, while $Sc_2Cu_2O_5$ could be very close to the critical boundary.

ACKNOWLEDGMENTS

The authors acknowledge Drs. M. Parras and M.Vallet-Regí for supplying the samples. Financial support from the Spanish CICYT-Midas (Mat: 91-0742) and DGICYT (PB92-0849) programs are acknowledged.

REFERENCES

1. J. G. Bednorz and K. A. Muller, *Z. Phys. B* **64,** 189 (1986).
2. Y. Tokura *et al.*, *Nature* **337,** 345 (1989).
3. J. F. Bringley, S. Trail, and B. Scott, *J. Solid State Chem.* **86,** 310 (1990).
4. M. Braden, W. Paulus, A. Cousson, P. Vigoureux, G. Heger, A. Goukassov, P. Bourges, and D. Petitgrand, *Europhys. Lett.* **25,** 625 (1994).
5. G. Bergerhoff and H. Kasper, *Acta Crystallogr. B* **24,** 388 (1968).
6. H. R. Freund and H. Müller-Buschbaum, *Z. Naturforsch. B* **32,** 609 (1977).
7. J. L. García-Muñoz, J. Rodríguez-Carvajal, X. Obradors, M. Vallet-Regi, J. Gonzalez-Calbet, and E. García, *Phys. Lett. A* **149,** 319 (1990).
8. J. Aride, S. Flandrois, M. Taibi, A. Boukhari, M. Drillon, and J. L. Soubeyroux, *Solid State Commun.* **72,** 459 (1989).
9. R. Troc, J. Klamut, Z. Bukowski, R. Horyn, and J. Stepien-Damm, *Physica B* **154,** 19 (1989).
10. J. L. García-Muñoz *et al.*, *Phys. Rev. B* **44,** 4716 (1991). J. L. García-Muñoz, X. Obradors, and J. Rodríguez-Carvajal, *Physica B* **194–196,** 277 (1994).
11. J. Rodríguez-Carvajal, "FULLPROF: A Program for the Rietveld Refinement and Pattern Matching Analysis." Abstracts of the Satellite Meeting on Powder Diffraction of the XV Congress of the International Union of Crystallography, Toulouse, France, 1990, p. 127.
12. A. Salinas-Sánchez, J. L. García-Muñoz, J. Rodríguez-Carvajal, R. Sáez-Puche, and J. L. Martínez, *J. Solid State Chem.* **100,** 201 (1992).
13. R. D. Shannon, *Acta Crystallogr. Sect. A* **32,** 751 (1976), I. D. Brown, *Acta Crystallogr. Sect. B* **48,** 553 (1992).
14. A. Murasik, P. Fischer, R. Troc, and Z. Bukowski, *Solid State Commun.* **75,** 785 (1990).
15. I. D. Brown, *Z. Kristallogr.* **199,** 255 (1992).
16. T. Armbruster, F. Röthlisberger, and F. Seifert, *Am. Miner.* **75,** 847 (1990).